Scientific Reports

https://doi.org/10.1038/s41598-026-42285-6

Article in Press

# Seepage characteristics of fractured sandstone under deep high-confined water and mining-induced stress

Received: 14 December 2025

Accepted: 25 February 2026

Published online: 01 March 2026

Cite this article as: Tu H., Wu R., Jia S. *et al.* Seepage characteristics of fractured sandstone under deep high-confined water and mining-induced stress. *Sci Rep* (2026). https://doi.org/10.1038/s41598-026-42285-6

**Hongsheng Tu, Runze Wu, Sheng Jia, Shangxin Fang & Cun Zhang**

# Seepage Characteristics of Fractured Sandstone under Deep High-Confined Water and Mining-Induced Stress

Hongsheng Tu[1], Runze Wu[2], Sheng Jia[2] Shangxin Fang[2], Cun Zhang[2]*

*1. School of Mines, China University of Mining and Technology, Xuzhou 221116, China*

*2. School of Energy & Mining Engineering, China University of Mining and Technology-Beijing, Beijing 100083, China*

*Corresponding author: cumt-zc@cumtb.edu.cn (Cun Zhang)*

**Abstract:** Under deep mining conditions, fractured rock masses are subjected to sustained high confining stress and elevated water pressure, resulting in complex seepage evolution. This study conducts triaxial seepage experiments on single-fractured sandstone to investigate the coupled effects of confining pressure, water pressure, fracture roughness (JRC), and fracture aperture under a unified stress–seepage framework representative of deep high-confined water environments. Results show that seepage flow increases linearly with water pressure but decreases nonlinearly with confining pressure, exhibiting a three-stage evolution involving elastic deformation, elasto-plastic transition, and compaction equilibrium, with a clear stabilization threshold. Elevated water pressure reduces the effective normal stress on fracture surfaces, thereby weakening fracture closure, particularly in rough fractures where asperity degradation contributes to permeability enhancement. Comparative analyses reveal that fracture roughness and aperture jointly control permeability magnitude, attenuation rate, and stabilization behavior. Quantitative relationships between stabilized permeability and key fracture parameters are established, providing a concise, parameter-based description of fracture seepage under high-stress conditions. The findings offer practical insights for predicting seepage evolution and mitigating floor water inrush risks in deep mining environments.

**Keywords:** High-Confined Water; Mining-induced stress; Joint roughness coefficient; Seepage characteristic; Fracture aperture

## Highlights:

1. Seepage flow shows a three-stage evolution with confining pressure: elastic deformation, elastoplastic transition, and compaction equilibrium, stabilizing above 10 MPa.
2. Fracture roughness (JRC) and aperture synergistically control seepage:

lower JRC and larger aperture yield higher initial flow but greater susceptibility to confining pressure-induced reduction.

3. The seepage-hydraulic gradient relationship is segmented into linear (Darcy-dominated) and nonlinear regimes (inertia-influenced), with deflection patterns varying by roughness.

# 1 Introduction

Deep mining is characterized by high in-situ stress and high confined-water pressure, which significantly alter the mechanical and seepage properties of floor rock strata[1]. As the working face advances, the redistribution of surrounding rock stress induces the initiation, propagation, and eventual penetration of mining-induced fractures[2]. These throughgoing fractures gradually evolve into highly efficient water-conducting channels, accelerating groundwater migration toward the goaf and consequently increasing the risk of catastrophic floor water inrush[3], as illustrated in Figure 1.

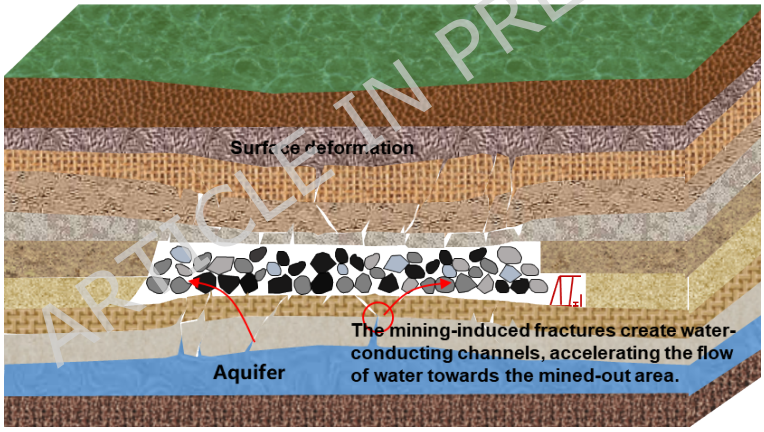


Figure 1. Disaster Modes of Floor Water Inrush in Deep Mining

With increasing mining depth, both tectonic stress and pore water pressure rise, and stress concentration caused by mining activities may activate structural planes and intensify the formation of throughgoing fractures[4]. Due to mining disturbances and geological variability, such fractures exhibit substantial differences in geometry, aperture, roughness, complexity, dip angle, orientation, and extension[5-8]. Consequently, extensive research has focused on the effects of fracture aperture, inclination, roughness, and loading conditions, yielding significant advances in understanding their control over seepage behavior[9-14].

Experimental studies have demonstrated that fracture-surface roughness

is a key factor influencing seepage capacity. Lin et al.[15] and Gan et al.[16] reported that under identical hydraulic pressure, higher roughness leads to lower permeability and more complex flow patterns within the fracture. Zhao et al.[17] established a quantitative relationship among relative roughness, fractal dimension, and microscopic structural parameters of fractures based on fractal theory and fundamental principles of fluid mechanics. Liu et al.[18] based on the fractal geometry correction of the cubic law, introduced the fractal dimension to characterize the nonlinear seepage of rough fractures. Numerical simulations conducted by Jia et al.[19] using COMSOL further confirmed the weakening effect of increasing roughness on flow capacity. Confining pressure and effective stress are also critical factors controlling fracture permeability. Fu et al.[20]found that increasing confining pressure compresses fracture aperture and reduces permeability, with rough fractures exhibiting stronger sensitivity to stress changes. Zhang et al.[21] showed that fracture flow velocity is negatively correlated with effective stress, and that variations in confining pressure and porosity significantly influence hydraulic conductivity. Gan et al.[22]reported pronounced roughness-controlled hysteresis in fracture permeability, although this effect weakens under high-stress conditions. Additionally, Zhang et al.[23]revealed that elevated pore water pressure enhances rock brittleness and reduces characteristic stress, whereas increasing confining pressure raises characteristic stress and accelerates fracture deformation. Chen et al.[24]observed that cyclic loading reduces coal fracture permeability by more than 50% and induces irreversible damage, and therefore proposed a “permeability recovery coefficient” to quantify mining-induced disturbances. Zha[25]further elucidated the coupled evolution of rock mechanical and seepage behavior through triaxial compression–seepage testing combined with MATLAB analysis.

In summary, although extensive studies have examined the effects of fracture roughness, loading conditions, and water pressure on throughgoing fracture seepage, most of the existing work focuses on single-factor influences. Systematic investigations considering the coupled effects of fracture roughness, aperture, seepage pressure, and confining pressure remain limited. To address the urgent need for preventing floor water inrush in deep mines, this study integrates seepage experiments on fractured rock masses with theoretical analysis to systematically investigate fracture seepage behavior under various stress–seepage coupling conditions, thereby providing

experimental support for understanding the floor water inrush mechanism under high confined-water pressure.

# 2 Engineering background and rock sample preparation

## 2.1 Engineering Background: Geological Setting of Xingdong Coal Mine

Xingdong Coal Mine is situated on the western edge of the North China Basin, with mining depths ranging from 1038 to 1271 meters, classifying it as a typical deep mine. The coal-bearing strata primarily consist of the Taiyuan Formation (Upper Carboniferous), Shanxi Formation (Lower Permian), and Benxi Formation (Middle Carboniferous). The mine lies in the eastern part of the Baichuan Hydrogeological Unit, which is a relatively independent and enclosed system. Multiple aquifers are distributed within the mining area, with five main aquifers identified below the floor of the #2 coal seam, as illustrated in Figure 2.

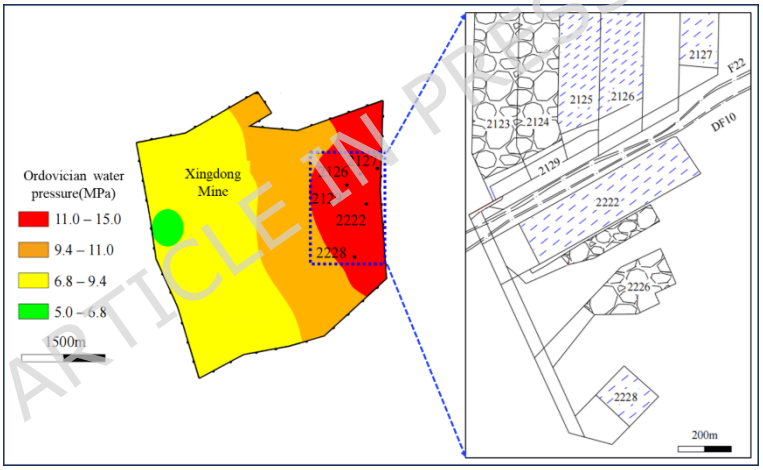


a. Water inrush working face in Xingdong Mine

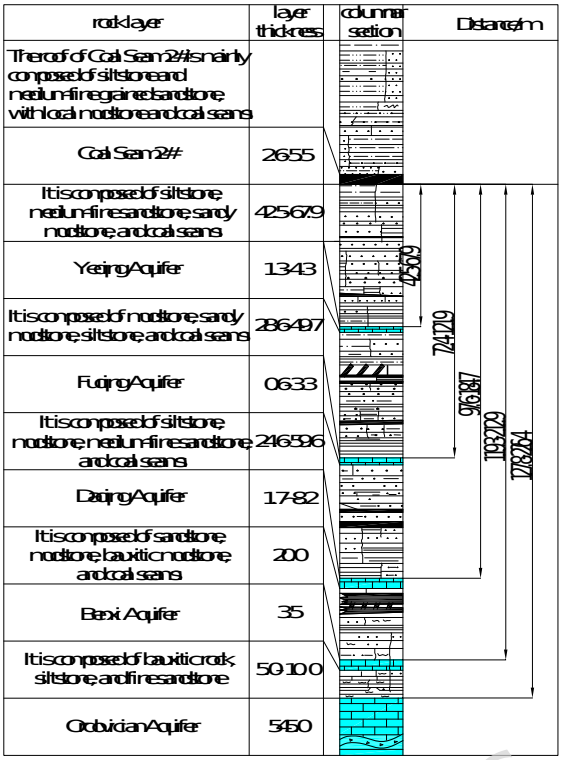


b. Comprehensive columnar section of floor rock strata

Figure 2. Water inrush working face and comprehensive columnar section of floor rock strata

The Ordovician limestone aquifer, serving as the basement of the coal-bearing strata, has a total thickness of 545 meters. Its water-bearing capacity is heterogeneous, with stronger water abundance in localized areas. Borehole water level benchmarks range from +25.35 to +35.95 meters, yielding maximum water pressures of up to 15 MPa and minimum pressures as low as 11 MPa. The top of the Ordovician limestone is located 123.76 to 193.14 meters from the #2 coal seam. While other aquifers exhibit weak water-bearing capacity and minimal mining-induced disturbance, the Ordovician limestone—with its high karstification, abundant water, and elevated pressure—poses a significant risk of floor water inrush during mining operations.

The floor of the #2 coal seam comprises five aquifer layers, mainly composed of medium- to fine-grained sandstone, siltstone, coal seams, sandy mudstone, aluminum-rich mudstone, and aluminum-rich siltstone. Among these, sandstone layers have relatively poor water-blocking capabilities. Additionally, the presence of numerous faults and collapse columns in the strata increases the susceptibility to water inrush incidents. To address the urgent need for understanding water inrush mechanisms, this study selects

sandstone from the #2 coal seam floor as the research object. This gray, low-permeability sandstone was drilled and polished into eight standard samples (50 mm diameter, 100 mm length) from the in-situ floor, as shown in Figure 3.

Figure 3. Processed sandstone rock sample

## 2.2 Rock Sample Preparation Procedure

All fractures in this study were generated to be approximately perpendicular to the specimen axis, such that fracture deformation was dominated by normal compression rather than shear displacement. This configuration was adopted to isolate the effects of confining pressure and seepage pressure on fracture closure and seepage evolution. To obtain sandstone samples with varying roughness, an auxiliary splitting device was employed to fracture the samples. The preparation process involved the following steps:

(1) Fabrication of Auxiliary Devices: Eight sets of auxiliary devices with different joint roughness coefficients (JRC) were manufactured. Each set comprised a pair of wedges and a support frame (Figure 4a). The wedges were crafted by inputting JRC values (0–20) into a computer, engraving corresponding curves onto stainless steel via a digital control machine, and enhancing stiffness through quenching and heat treatment.

(2) Sample Splitting: Using the auxiliary splitting device, the sandstone samples were split into two halves (Figure 4b), ensuring that the angle between the fracture surface normal and the sample axis was $\leq 2°$. The support frame maintained consistent orientation, so even with different wedges, the average fracture surface remained perpendicular to the cylindrical ends.

(3) Sample Selection: Five groups of fractured samples (Figure 4c) with distinct roughness levels were selected for seepage experiments.

This method ensured controlled fracture geometry, providing standardized

samples for subsequent seepage characterization. The prepared samples were then sealed and assembled for testing. The rigorous preparation protocol guarantees reproducibility and relevance to in-situ conditions, facilitating accurate analysis of seepage behavior under high-confined water and mining-induced stress.

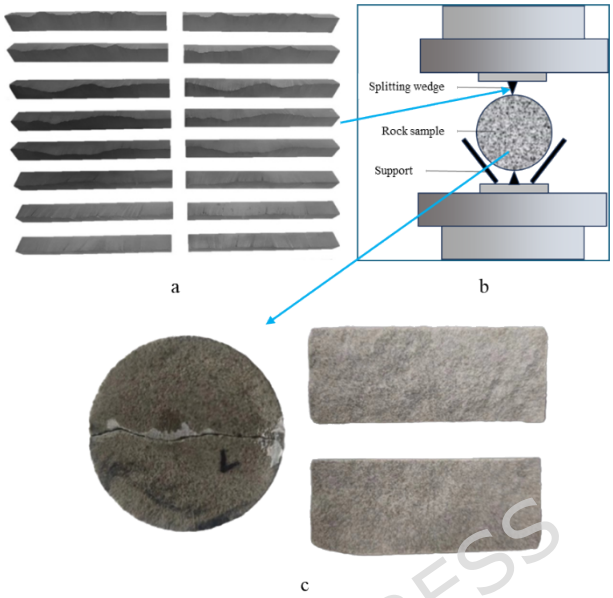


Figure 4. Process Diagram for Preparation of Single Fractured Rock Sample: a shows the splitting wedge shape, b represents the auxiliary splitting device, and c depicts the rock sample after splitting and the fracture surface.



## 3 Fracture Surface Scanning and Roughness Calculation

This section details the procedures for acquiring and quantitatively characterizing the morphology of fracture surfaces in rock samples. Accurate measurement of surface roughness is essential for understanding its influence on seepage behavior. The process involves two main steps: three-dimensional scanning of fracture surfaces and computational assessment of the Joint Roughness Coefficient (JRC).

### 3.1 3D Scanning of Rock Sample Fracture Surfaces

A non-contact optical 3D scanner was employed to capture the precise morphology of the fracture surfaces and the overall sample geometry. This equipment, with an accuracy of 0.005–0.015 mm, a 5-megapixel resolution, and a point spacing of 0.04–0.16 mm, rapidly acquires high-resolution spatial data (single measurement time $\leq$ 1.5 seconds) over a maximum detection area of 400 $\times$ 300 mm$^2$. The raw scan data was processed using Geomagic Studio

software to generate a 3D digital model. A coordinate system was established within this model, allowing the fracture surface to be isolated, plotted as a scatter diagram, and its coordinate data exported for further analysis, as illustrated in Figure 5.

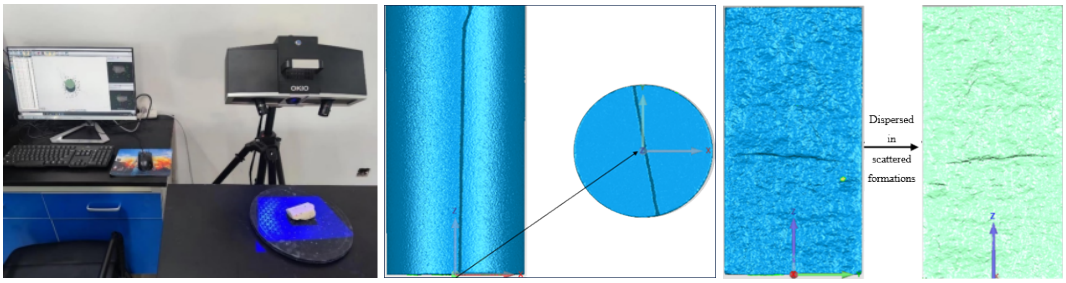


Figure 5. 3D Scanning Equipment and Model Diagram

### 3.2 Characterization of Fracture Surface Roughness

The Joint Roughness Coefficient (JRC) is a widely adopted parameter for quantitatively describing fracture surface roughness. The 3D coordinate data obtained from scanning were processed using Surfer software to generate a digital image of the fracture surface, as shown in Figure 6. The JRC values were then calculated using Equations (1) and (2). Based on the calculated JRC, the five groups of fractured rock samples were designated A1 through A5, with corresponding values listed in Table 1.

$$Z_{2s} = \left[\frac{1}{(N_x-1)(N_y-1)}\sum_{i=1}^{N_x-1}\sum_{j=1}^{N_y-1}\frac{(Z_{i-1,j-1}-Z_{i-1,j})^2+(Z_{i-1,j}-Z_{i,j})^2}{2Dx^2}+\sum_{i=1}^{N_x-1}\sum_{j=1}^{N_y-1}\frac{(Z_{i-1,j-1}-Z_{i-1,j})^2+(Z_{i,j-1}-Z_{i,j})^2}{2Dy^2}\right]^{\frac{1}{2}} \quad (1)$$

$$JRC = 32.2 + 32.47 \log Z_{2s} \quad (2)$$

where $Z_{2s}$ represents the average gradient modulus of the basic plane of the joint surface, $Z_{ij}=Z(x_i, y_j)$; $N_x$ and $N_y$ represent the number of grid points along the x-axis and y-axis respectively; $\Delta x$ and $\Delta y$ represent the grid step sizes along the x-axis and y-axis respectively; $L_x$ and $L_y$ represent the nominal lengths along the x-axis and y-axis respectively. $Lx = (N_x - 1)\ x$, $L_y = (N_y - 1)\ y$, and $JRC$ is the fracture roughness coefficient. This systematic characterization provides a quantitative basis for analyzing the correlation between surface morphology and seepage characteristics in the subsequent sections. The JRC values in this study were calculated based on high-resolution three-dimensional scanning data, providing a quantitative and repeatable characterization of fracture surface roughness. Compared with visual matching to the Barton standard profiles, the scanning-based approach

reduces subjectivity and ensures consistency among different samples. It should be noted that the absolute JRC values may be affected by scanning resolution; however, all fracture surfaces were scanned under identical conditions, and the scanning resolution was sufficiently smaller than the characteristic asperity size. Therefore, the calculated JRC values are considered reliable for relative comparison and trend analysis within the scope of this study.

Table 1 Value Table of Rock Sample Joint Roughness Coefficient (*JRC*)

| Rock sample number | JRC value |
|---|---|
| A1 | 0.87 |
| A2 | 2.24 |
| A3 | 8.74 |
| A4 | 11.21 |
| A5 | 19.22 |

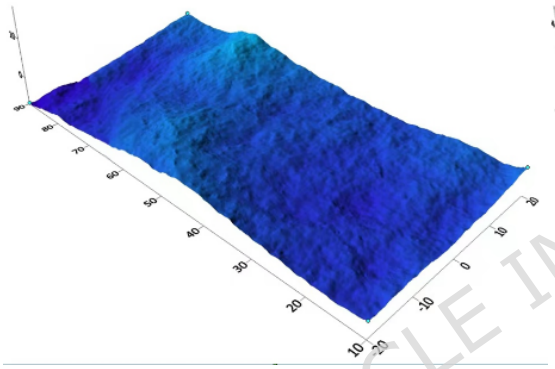

(a) A1 rock sample

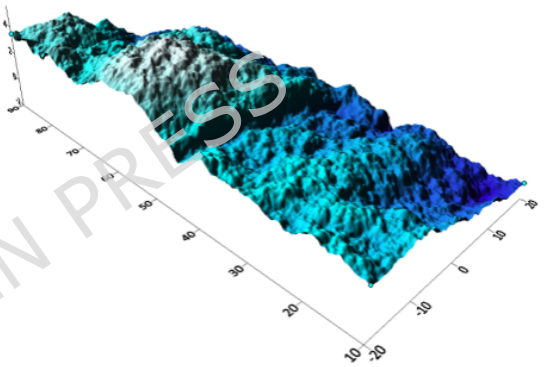

(b) A2 rock sample

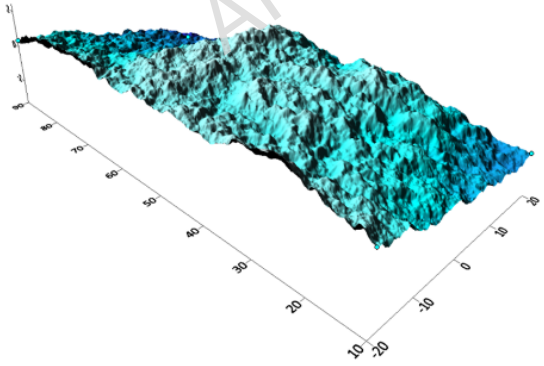

(c) A3 rock sample

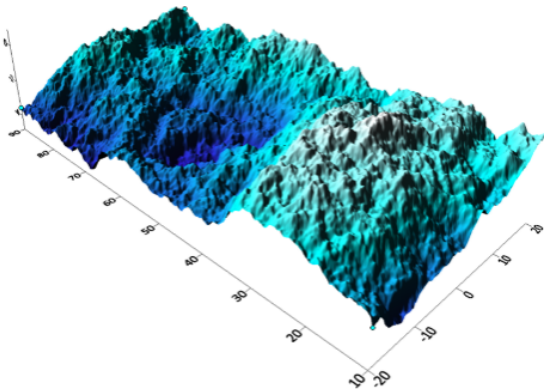

(d) A4 rock sample

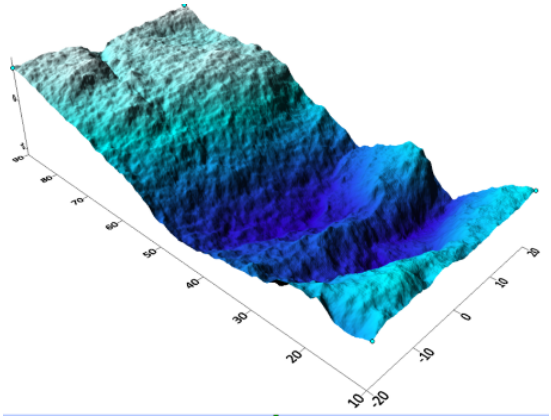

(e) A5 rock sample

Figure 6. Digital image of fracture surface with different JRC

# 4 Experimental Procedure and Scheme for Fracture Seepage

This section details the experimental system, methodology, and testing scheme employed to investigate the seepage characteristics of fractured sandstone under coupled stress-seepage conditions. The procedure ensures controlled and reproducible measurements of flow behavior under varying confining pressures, water pressures, and fracture geometries.

## 4.1 Experimental System and Setup

The seepage experiments were conducted using a small-scale conventional triaxial multi-field coupling experimental system for rocks, as illustrated in Figure 7. This system integrates independent loading systems for confining pressure and axial pressure, controlled by high-precision constant-speed pumps. It is specifically designed for studying the thermo-hydro-mechanical coupling characteristics of rocks and fractured rock masses, including permeability and hydraulic fracturing experiments. Key system parameters include: (1) Pressure Loading Range: 0–70 MPa for the displacement pump, confining pressure pump, and axial pressure pump. (2) Pressure Accuracy: 0.01 MPa for each pump. (3) Flow Rate Range: 0–100 mL/min (displacement pump), 0–30 mL/min (confining pressure pump), and 0–30 mL/min (axial pressure pump).

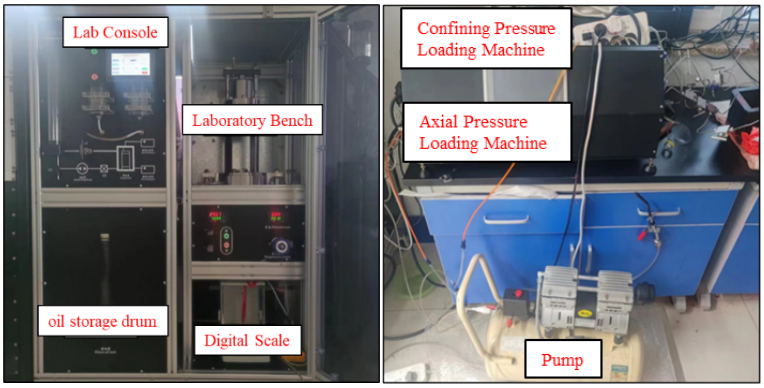


(a)Experimental pressure loading system

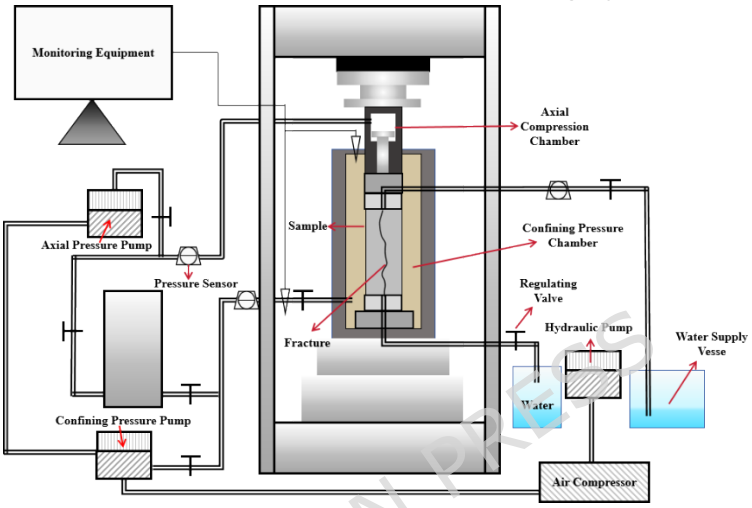


(b) Principle diagram of the seepage experiment equipment

Figure 7. Triaxial hydrodynamic coupling experiment device

## 4.2 Sample Preparation and Sealing

Prior to testing, the fractured rock samples were prepared to ensure one-dimensional flow through the fracture: (1) Fracture Sealing: External fractures on the rock samples were sealed with a colloidal compound to prevent water from bypassing the main fracture along the sample's outer surface, which could compromise the experimental results. (2) Heat Shrinking: A heat-shrink tube (0.5 mm thick, 55 mm inner diameter) was placed over the sealed sample. Using a hot air gun, the tube was shrunk tightly onto the sample's surface, providing a robust and waterproof seal, as shown in Figure 8. (3) Sample Installation: The prepared rock sample was instrumented with sensors and securely fixed onto the experimental platform, as depicted in Figure 9.

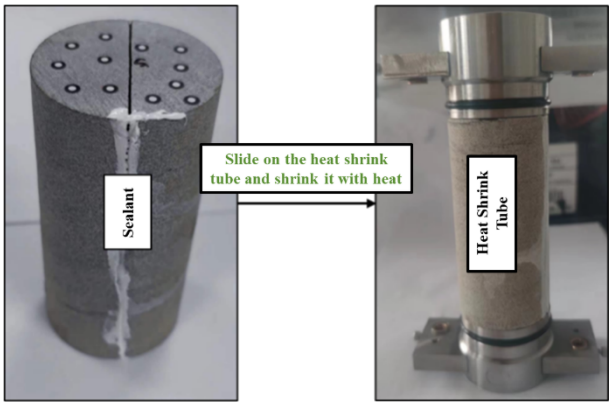


Figure 8. Rock samples after heat treatment


Figure 9. Rock sample after fixation



### 4.3 Experimental Procedure

In this study, the term “mining-induced stress” refers to the elevated stress environment and associated effective stress changes caused by deep mining activities, rather than a direct simulation of anisotropic mining stress paths. Accordingly, an isotropic and monotonic loading scheme was intentionally adopted to investigate the fundamental seepage evolution of fractured sandstone under sustained high confining pressure and water pressure. This simplified loading path was designed to isolate the dominant effects of confining pressure and seepage pressure on fracture compaction and seepage behavior, and to establish a baseline understanding of stress-controlled seepage evolution, rather than to directly reproduce stress relief, repeated disturbances, or shear-dominated processes induced by mining operations. The seepage test was performed on five groups of fractured rock samples (A1-A5). Data recording commenced only after the measured seepage rate stabilized. The core experimental procedure consisted of the following steps:

(1) Initial Loading: The axial pressure was gradually increased until the rock sample was fully compacted, then set to 1 MPa. The inlet and outlet pipes

were connected to the sensing device.

(2) Chamber Closure and Confining Pressure Application: The experimental chamber was sealed, and the confining pressure was set to 1 MPa, maintaining equality with the axial pressure ($\sigma_1 = \sigma_3 = 1$ MPa).

(3) Water Pressure Cycling: The water pressure was gradually increased in increments. The seepage data (flow rate) were recorded at each water pressure level. After applying all designated pressure levels, the water pressure was reduced to 0 MPa.

(4) Stress Level Increase: Both the axial pressure and confining pressure were simultaneously increased to the next predefined level, maintaining $\sigma_1 = \sigma_3$. After pressure stabilization, Step 3 was repeated.

(5) Test Termination: Steps 3 and 4 were iterated until the axial and confining pressures reached the maximum preset value of 29 MPa, concluding the test for that sample group.

(6) Sample Replacement: The axial and confining pressures were removed, the equipment was depressurized, and the rock sample was replaced for the next test.

The specific experimental scheme, detailing the sequence of water pressure application at each confining pressure level, is summarized in Table 2.

Table 2 Experimental Plan Table

| Samples | Axial and confining pressure (MPa) | Osmotic pressure (MPa) |
|---|---|---|
| Five groups of rock samples with different degrees of roughness | 1 | 0, 0.05, 0.1, 0.2…0.6, 0.7 |
| | 2 | 0, 0.05, 0.1, 0.2, 0.4…1.4, 1.6 |
| | 3 | 0, 0.05, 0.1, 0.2, 0.5…2, 2.3 |
| | 4 | 0, 0.05, 0.1, 0.2, 0.5, 1…2.5, 3 |
| | 5 | 0, 0.05, 0.1, 0.2, 0.5, 1…3.5, 4 |
| | 6 | 0, 0.05, 0.1, 0.2, 0.5, 1…4, 5 |
| | 8 | 0, 0.05, 0.1, 0.2, 0.5, 1, 2…5, 6 |
| | 10 | 0, 0.05, 0.5, 1, 2…7, 8 |
| | 12 | 0, 0.05, 0.5, 1, 2…9, 10 |
| | 14 | 0, 0.1, 0.5, 2…10, 12 |
| | 16 | 0, 0.5, 1, 2, 4…12, 14 |
| | 18 | 0, 1, 2, 4…14, 16 |
| | 20 | 0, 1, 2, 4…16, 18 |
| | 23 | 0, 1, 2, 4…16, 18 |
| | 26 | 0, 1, 2, 4…16, 18 |
| | 29 | 0, 1, 2, 4…16, 18 |

### 4.4 Supplementary Experiments

Two additional sets of experiments were conducted to investigate specific effects: (1) Time-Dependent Permeability: The five original rock samples (A1-A5) were dried. A seepage experiment was then conducted under a constant confining pressure of 5 MPa and a water pressure of 0.5 MPa for 24 hours to observe the temporal evolution of permeability. (2) Fracture Aperture Effect: Five new fractured rock samples, all with a similar JRC value of 11.21, were prepared and labeled Y1-Y5. With the osmotic pressure set at 0.5 MPa and a test temperature of 20°C, the initial fracture aperture was precisely controlled using a displacement sensor by adjusting the confining pressure. The apertures for samples Y1 to Y5 were set at 0 mm, 0.05 mm, 0.1 mm, 0.15 mm, and 0.2 mm, respectively. Seepage experiments were performed to isolate the influence of fracture aperture on permeability.

This comprehensive experimental scheme is designed to systematically elucidate the coupled effects of confining pressure, water pressure, fracture roughness, and fracture aperture on the seepage behavior of fractured sandstone.

## 5 Analysis of experimental results

This section presents a detailed analysis of the experimental results, examining the seepage characteristics of fractured sandstone under the coupled influences of confining pressure, water pressure, fracture roughness (JRC), and fracture aperture. The permeability $k$ is calculated using the following formula, which is applied throughout the analysis:

$$k=\frac{h\mu L\Delta Q}{A\Delta P} \tag{3}$$

Where $A$ represents the cross-sectional area of the sample, $m^2$; $k$ represents the average permeability of each measurement point in the rock sample, $10^{-15}m^2$; $\eta$ represents the fluid viscosity coefficient, and it is set as $\eta = 1 \times 10^{-3}$ Pa·s (at water temperature of 20℃). $\Delta Q$ represents the infiltration volume passing through the sample within the time interval of $\Delta t$, $m^3$; $L$ represents the length of water flow infiltration, which is equivalent to the height of the sample in the test, m; $\Delta P$ represents the pressure difference between the upper and lower ends of the sample, Pa□

### 5.1 Seepage Characteristics Under the Influence of Effective Stress

Figure 10 illustrates the variation of seepage flow with confining pressure under different water pressures for fractured rock samples. The results demonstrate a clear coupling effect between water pressure and confining pressure: At a constant confining pressure, seepage flow increases significantly with rising water pressure, indicating enhanced driving force for fluid flow through the fractures. At a constant water pressure, seepage flow decreases nonlinearly as confining pressure increases, eventually stabilizing at higher pressures. This stabilization occurs because fracture closure approaches a limiting state under high confining stress. The confining pressure required to induce a significant decrease in seepage flow rises with increasing water pressure. For instance, at a water pressure of 0.5 MPa, a notable decrease occurs at ~4 MPa confining pressure, whereas at 5 MPa water pressure, the threshold increases to ~8 MPa. This indicates that high water pressure can partially counteract the fracture-closing effect of confining pressure.

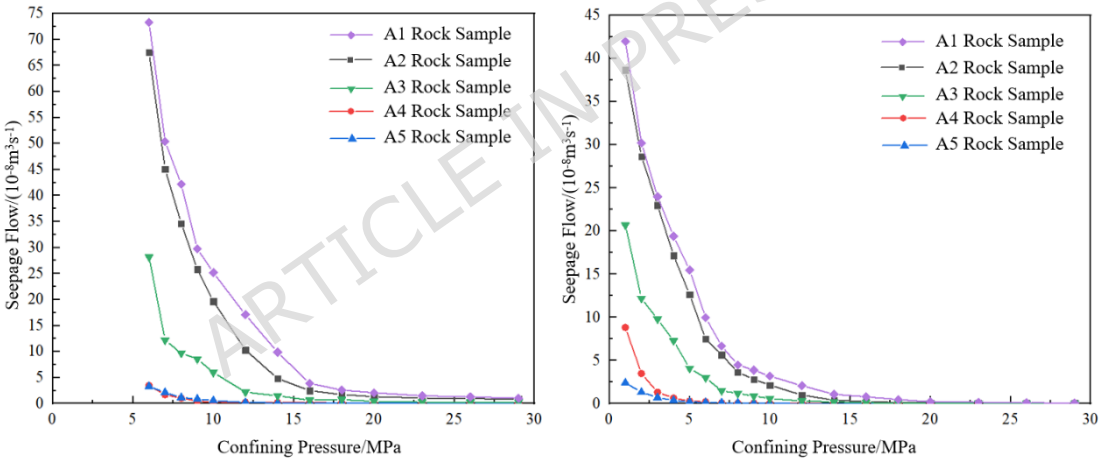


(a) Water pressure: 0.5 MPa (b) Water pressure: 1 MPa

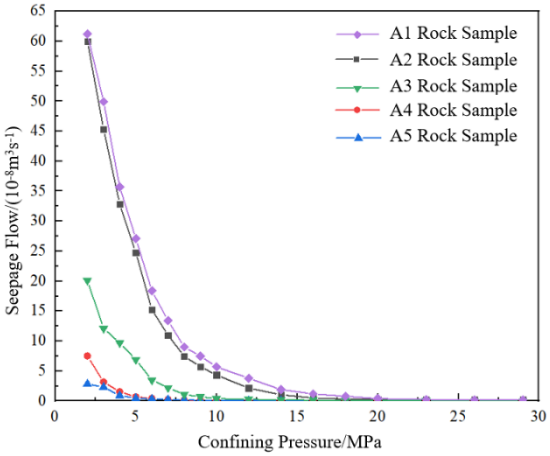


(c) Water pressure: 5 MPa

Figure 10. Seepage flow variation with confining pressure for different rock samples

The experimental results demonstrate that the seepage flow rate of fractured sandstone exhibits a clear stress-dependent evolution under coupled confining pressure and water pressure conditions. At relatively low confining pressures, the seepage flow rate decreases rapidly due to progressive fracture closure induced by normal stress. With further increase in confining pressure, the reduction rate of flow gradually diminishes, and the seepage behavior tends to stabilize when the confining pressure exceeds approximately 4–10 MPa.

Water pressure serves as the primary driving force for seepage and significantly weakens the restraining effect of confining pressure on fracture closure. An increase in water pressure reduces the effective normal stress acting on fracture surfaces, resulting in an enhancement of seepage flow capacity. This enhancement effect is more pronounced for fractures with higher roughness (JRC), where asperity interaction and local shear damage contribute to sustained flow channels.

In addition, fracture roughness and aperture jointly influence the magnitude of seepage flow and its sensitivity to stress conditions. Although the seepage flow rate under different test conditions follows similar overall trends, notable differences exist in attenuation amplitude and threshold behavior, reflecting the combined influence of stress state and fracture structural characteristics. This flow-based characterization provides a concise and physically meaningful description of fracture seepage behavior with clear engineering relevance.



The decline rate of permeability with confining pressure, plotted in Figure 11, reveals a three-stage evolution process:

(1) Elastic Deformation Stage (Confining Pressure < 4 MPa): Permeability decreases rapidly (e.g., decline rates near $2\times10^{-15}$m$^2$/MPa for A1-A3). The asperities on the fracture surfaces undergo elastic deformation, leading to a swift increase in contact area and rapid closure of flow channels.

(2) Elasto-Plastic Transition Stage (4 MPa ≤ Confining Pressure ≤ 10 MPa): The rate of permeability decline slows and exhibits fluctuations (decline rates near $0.3\times10^{-15}$m$^2$/MPa). Asperities begin to yield plastically, and the fracture structure undergoes rearrangement.

(3) Compaction Equilibrium Stage (Confining Pressure > 10 MPa): The fracture compaction limit is approached. The permeability decline rate

diminishes to less than $0.1\times10^{-15}m^2$/MPa as the reactive force between the fracture surfaces balances the applied confining pressure.

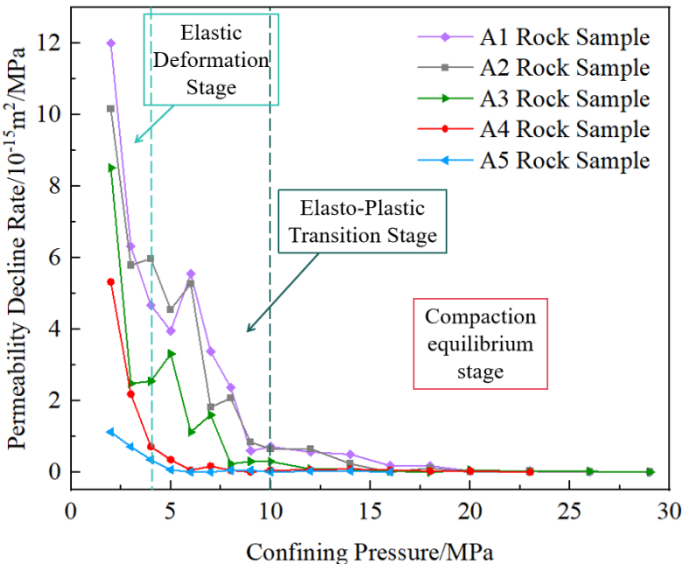


Figure 11. Rate of permeability decline for different JRC rock samples

## 5.2 Seepage Characteristics of Rock Samples with Different Roughness

Figure 12 presents the relationship between flow rate and hydraulic gradient for the five sample groups (A1-A5) under various confining pressures. The curves exhibit distinct segmentation: A linear regime at low hydraulic gradients, where flow rate increases linearly with gradient, consistent with Darcy-type laminar flow. At high hydraulic gradients, the flow rate–hydraulic gradient relationship exhibits a nonlinear behavior, which is attributed to the increasing contribution of inertial effects and dynamic adjustments of the fracture aperture. It should be noted that this nonlinear flow does not necessarily indicate fully developed turbulence; instead, it is more reasonably interpreted as inertia-influenced non-Darcy flow (Forchheimer-type flow) under confined fracture conditions[10].

Furthermore, the nonlinear segment displays different deflection patterns depending on the fracture roughness: (1) Deflection toward the X-axis: The flow rate increase decelerates with increasing gradient, indicating growing flow resistance. (2) Deflection toward the Y-axis: The flow rate accelerates, suggesting the opening of seepage channels. (3) Combined deflection (first X, then Y): An initial deceleration is followed by acceleration, reflecting a shift in the dominant seepage mechanism.

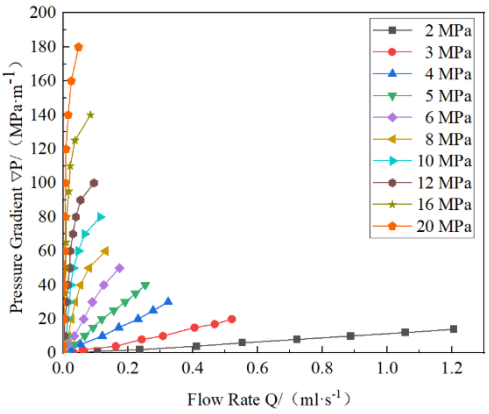


(a) A1 rock sample

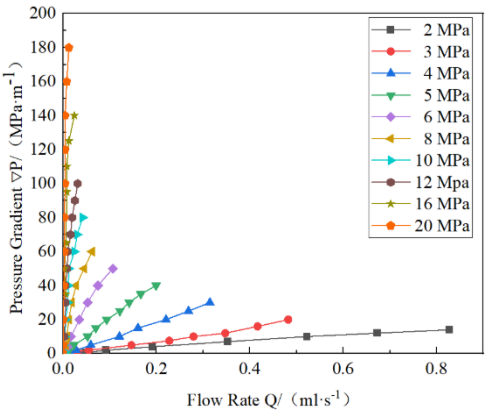


(b) A2 rock sample

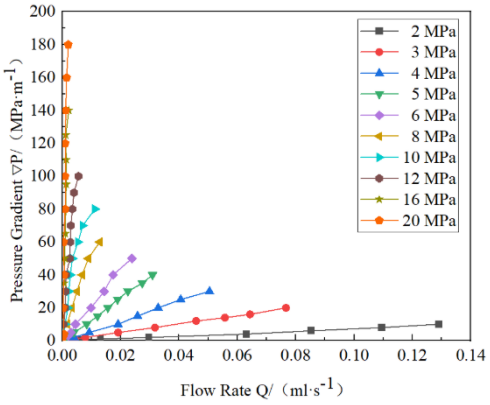


(c) A3 rock sample

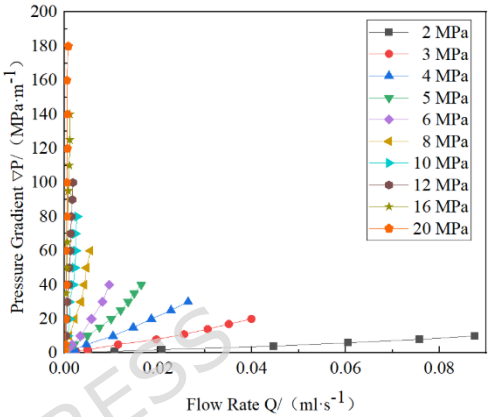


(d) A4 rock sample

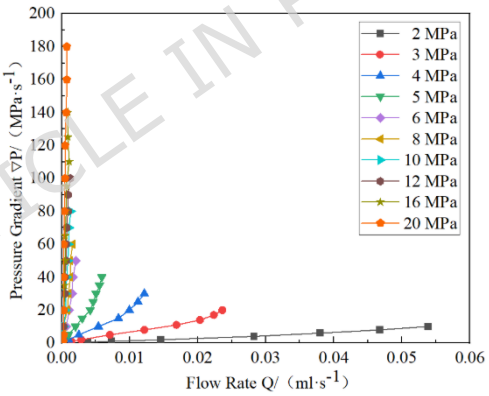


(e) A5 rock sample

Figure 12. Relationship between flow rate and pressure gradient of 5 groups of rock samples under different confining pressure conditions

Roughness significantly controls the absolute flow rate. Under identical confining pressure (e.g., 2 MPa) and hydraulic gradient (e.g., 10 MPa/m), the flow rate decreases substantially as JRC increases. For instance, the flow rate for sample A1 (JRC = 0.87) was 0.887 mL/s, while samples A2 through A5 showed reductions of 41.1%, 85.45%, 90.12%, and 93.9%, respectively. This is attributed to the longer, more tortuous flow paths and smaller effective cross-sectional areas in rougher fractures. The time-dependent evolution of

permeability under a constant confining pressure of 5 MPa and water pressure of 0.5 MPa is shown in Figure 13. The permeability of all samples decreased over 24 hours before stabilizing. Samples with lower JRC exhibited higher initial permeability ($k_c$) but also experienced greater absolute reduction ($\Delta k$). The stabilized permeability ($k_w$) values followed a decreasing trend with increasing JRC.

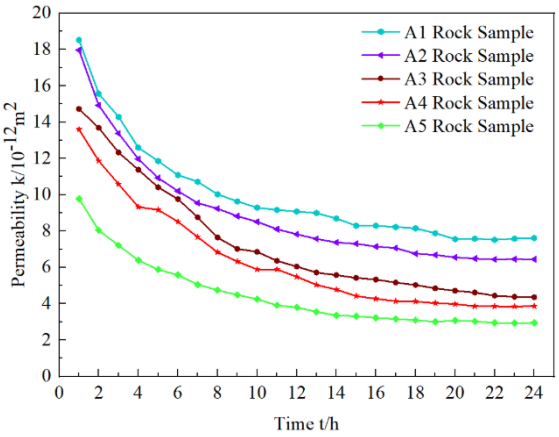


Figure 13. Curve showing the variation of rock sample permeability k for different JRCs

The relationship between stabilized permeability $k_w$ and JRC was successfully fitted with a high correlation coefficient ($R^2 = 0.9893$), as shown in Figure 14 and Equation (4). It should be noted that this fitting is derived from a limited number of JRC values and is intended to describe the observed trend under the present experimental conditions, rather than to serve as a universal predictive model.

$$k_w = 1.04851 + \frac{48.0637}{6.4923 + JRC} \quad R^2=0.9893 \qquad (4)$$

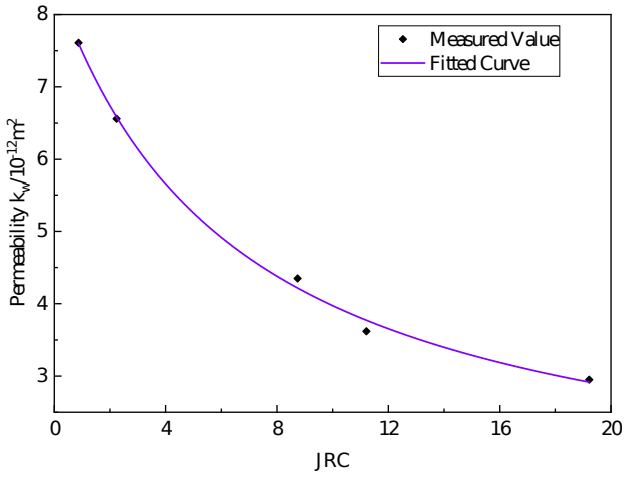


Figure 14. The fitted relationship between the stabilized permeability $k_w$ and JRC

This equation quantitatively captures how roughness reduces permeability by increasing the fractal dimension of flow paths. The term 1/JRC reflects the dominance of tortuosity—as JRC increases, the effective hydraulic aperture decreases nonlinearly due to greater contact areas. The model provides a practical tool for predicting long-term permeability in field conditions, where JRC can be estimated from borehole logs or geophysical data. For example, in the Xingdong Coal Mine, fractures with JRC > 10 (e.g., A5) would exhibit permeability below $2 \times 10^{-15}\text{m}^2$, significantly reducing water inrush risks compared to smoother fractures.

The findings highlight that roughness acts as a dual-edged sword: while it reduces initial seepage capacity, it also enhances fracture resilience under stress. Smoother fractures (low JRC) offer higher initial conductivity but are more vulnerable to confining pressure-induced closure, making them high-risk pathways for water inrush. Rougher fractures (high JRC), though less permeable, maintain stability under high stress due to their complex interlocking structure. This has direct implications for mining safety: in deep high-confined water environments, regions with smooth fractures (e.g., tectonic zones) require reinforced monitoring, whereas rough fractures may naturally inhibit flow amplification.

### 5.3 Influence of Fracture Aperture on Permeability

The effect of initial fracture aperture ($D$) was isolated using samples Y1-Y5 (with similar JRC ≈ 11.21) but different controlled apertures. The changes in permeability are summarized in Table 3.

Table 3 Changes in Permeability of Rock Samples with Different Fracture Aperture

| $K(10^{-12}\text{m}^2)$ | Y1 | Y2 | Y3 | Y4 | Y5 |
|---|---|---|---|---|---|
| Initial permeability $k_c$ | 39.84 | 53.42 | 66.59 | 79.23 | 103.74 |
| Stable permeability $k_w$ | 3.17 | 8.86 | 15.03 | 20.92 | 27.01 |
| $\Delta k=k_c-k_w$ | 36.67 | 44.56 | 51.56 | 58.31 | 76.73 |

The results indicate that both initial and stabilized permeability increase with larger aperture. However, the growth is sub-linear relative to the cubic law prediction. When the aperture increased fourfold (from 0.05 to 0.2 mm), $k_c$ increased by 94%, while $k_w$ increased by 205%, and the absolute permeability loss $\Delta k$ more than doubled. This indicates that wider fractures, while offering higher initial conductivity, are also subject to greater absolute

reductions under effective stress.

The temporal evolution of permeability (Figure 15) shows a rapid initial decline, followed by a slower decay until stabilization. The time required to reach stabilization increased with larger aperture (Y5 took 3.2 times longer than Y2), as wider fractures delay pressure equilibration due to fluid inertial effects.The stabilized permeability $k_w$ shows a strong positive correlation with the fracture aperture $D$, as illustrated by the fitting curve in Figure 16 ($R^2$ = 0.9911). This relationship provides a practical means for estimating long-term permeability based on initial fracture geometry.

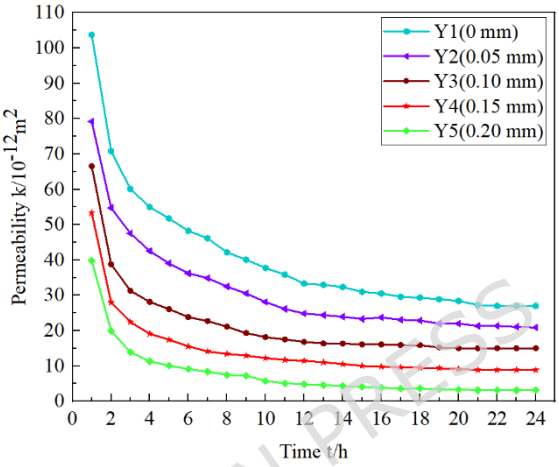


Figure 15. Permeability variation of rock samples with different fracture apertures

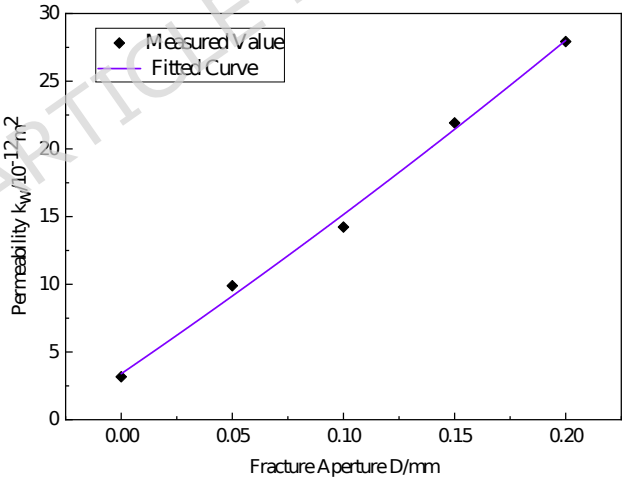


Figure 16. The fitting relationship between the stable permeability $k_w$ and the fracture aperture $D$

The strong dependence of permeability on aperture has direct relevance to water inrush prevention in deep mines like Xingdong. Fractures with larger initial apertures (e.g., tectonic faults or mining-induced fractures) pose higher short-term risks due to elevated initial flow, but their permeability stabilizes at lower values under high confining pressures (>10 MPa). This suggests that regions with wide fractures may require immediate support measures (e.g.,

grouting) to mitigate rapid water inflow, whereas long-term monitoring should focus on aperture stability under cyclic loading. Additionally, the time-delay in permeability stabilization for wide fractures highlights the need for extended observation periods in risk assessments.

# 6 Discussion

This section provides a comprehensive discussion on the underlying mechanisms governing the seepage behavior observed in the experiments. The analysis focuses on the coupling effect between water pressure and confining pressure, and the influential mechanism of fracture roughness, integrating the experimental findings with theoretical principles.

## 6.1 Mechanism of the Coupling Effect Between Water Pressure and Confining Pressure

The seepage characteristics of fractured rock samples are governed by the synergistic action of confining pressure and hydraulic pressure. Under their combined influence, the asperities on the fracture surfaces undergo compression and damage, leading to a progressive reduction and eventual closure of the flow paths within the fracture.

When the confining pressure is held constant, the seepage flow demonstrates a linear increase with rising water pressure. This relationship adheres to the fundamental principle of Darcy's law. Specifically, an increase in water pressure from 0.5 MPa to 5 MPa in our experiments resulted in an average 8 to 10-fold increase in seepage flow. From a fluid mechanics perspective, this phenomenon can be attributed to the enhanced pressure gradient ($\nabla P$), which serves as the driving force for fluid flow through the rock fractures, as described by the Navier-Stokes equation[26]:

$$\nabla P = \mu \nabla^2 v \tag{5}$$

where $\mu$ represents the dynamic viscosity of the fluid and $v$ represents the flow velocity. The increased pressure gradient consequently enhances the flow rate and the volumetric seepage flow.

Conversely, when the water pressure is constant, the seepage flow exhibits a characteristic exponential decay with increasing confining pressure. Based on the principles of elastic mechanics, the relationship between fracture closure ($\Delta b$) and effective stress can be expressed as:

$$\Delta b = b_0 - b = \left(\frac{s}{k_n}\right)^m \tag{6}$$

Where $b_0$ represents the initial fracture aperture, $k_n$ denotes the normal stiffness of the fracture, and $m$ is an empirical index (adopted as 0.7 in this study). This equation indicates that as confining pressure increases, the effective stress increases, leading to greater fracture closure, a reduced hydraulic aperture, narrowed flow channels, and significantly decreased permeability. However, a threshold effect for confining pressure loading was observed during the experiments. Once this threshold is exceeded, changes in seepage flow stabilize, signifying that the contact deformation on the fracture surfaces has entered a stage where further loading has a diminished impact on the fracture aperture and, correspondingly, on the permeability.

As summarized in Section 5.1, the evolution of fracture seepage under confining pressure can be categorized into three distinct stages, as illustrated in Figure 17, each associated with different mechanical deformation characteristics:

(1) Elastic Deformation Stage: At confining pressures below 4 MPa, permeability declines steeply. The interlocking asperities on the fracture surfaces undergo elastic deformation, leading to a rapid increase in contact area, a reduction in fracture aperture, and a swift contraction of the flow channels. The number of fragmented particles within the fractures increases, significantly augmenting fluid flow resistance and accelerating the rate of permeability decline.

(2) Elasto-Plastic Transition Stage: Within the confining pressure range of 4 MPa to 10 MPa, the rate of channel contraction slows and exhibits fluctuations. The corresponding permeability decline is slower and fluctuating. During this stage, the asperities experience plastic deformation and localized crushing occurs. The mobilized particles gradually become fixed due to spatial constraints.

(3) Compaction Equilibrium Stage: When the confining pressure exceeds 10 MPa, the limit of fracture compaction is approached. The contact area between the fracture surfaces reaches a critical state, achieving mechanical equilibrium. The deformation and aperture of the fracture surfaces stabilize, leading to a stabilization of permeability. The rate of permeability decline gradually diminishes to a minimal value.

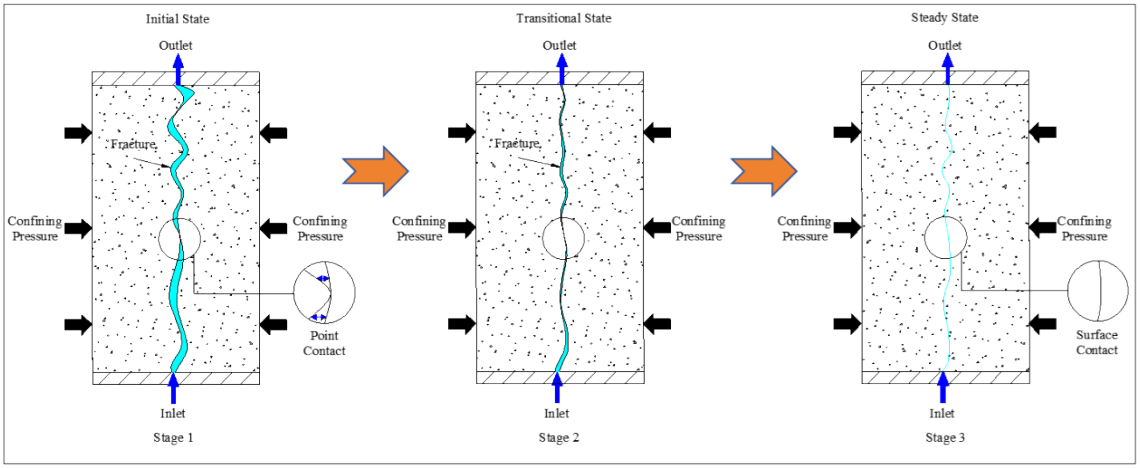


Figure 17. Evolution Process Diagram of Fracture Seepage

## 6.2 Mechanism of the Influence of Roughness on Seepage

The long-term evolution of permeability in fractures with different Joint Roughness Coefficient (JRC) values exhibits significant differences, as depicted in Figure 18. The permeability decline curves and the associated mechanisms reveal the critical role of surface morphology.

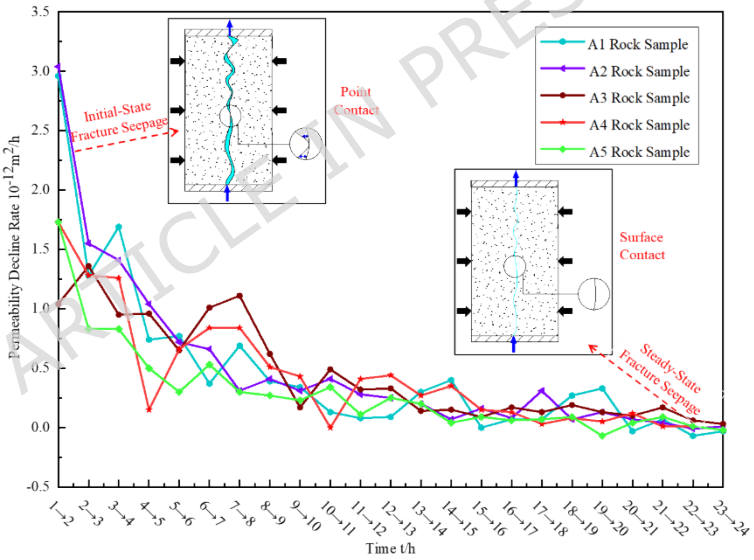


Figure 18. Curve of permeability decline for different JRC fractures and mechanism diagram

Analysis of the curve changes indicates that for fractures with lower JRC values (smoother surfaces), permeability decreased by approximately 46% during the 24-hour seepage test. In these fractures, the initially smooth surfaces facilitate the transport of fine particles (e.g., clay minerals) by the fluid, which can lodge within and block the flow channels, leading to a permeability reduction. The quantity of transported particles is linearly related to the flow velocity. Rapid pore-filling occurs initially, and once

approximately 50% of the pores are filled, the remaining pore structure stabilizes, and the seepage rate of the fractures consequently stabilizes.

In contrast, the permeability of fractures with high JRC values (rougher surfaces) can decrease by up to 70%. This more pronounced reduction is attributed to a dynamic process involving both wear and filling. The protrusions on the rough fracture surfaces are abraded by the fluid flow, which can temporarily increase the fracture aperture. However, this process simultaneously generates new debris particles that subsequently fill the fractures, reducing the effective flow area. This results in a rapid initial decrease in permeability. As the protrusions wear down to a certain extent and the particle size distribution stabilizes, the rate of permeability decrease slows and eventually stabilizes. This indicates that fracture roughness not only governs the initial seepage characteristics but also exerts a profound influence on the long-term seepage behavior, involving a complex interplay between mechanical wear and particle migration.

For future research, it is recommended to further refine the quantitative relationship between fracture plastic deformation and particle migration under varying confining pressure gradients to clarify the dynamic coupling path of confining pressure-deformation-seepage. Furthermore, in-depth studies could investigate the effects of different fluid media (e.g., fluids with varying chemical compositions and particle sizes) on the evolution of permeability in fractures with different JRC values. For instance, research could explore whether acidic fluids alter fracture surface roughness through chemical corrosion and thereby affect flow laws, or whether the transport and deposition mechanisms of different-sized particles within fractures lead to new characteristics in permeability evolution. Coupling multiple fields, such as temperature-seepage coupling in complex environments, could reveal further changes in the flow characteristics of fractures in different JRC rock samples. Subsequently, combining these findings with numerical simulation to establish a JRC evolution seepage model could enable accurate prediction of the long-term seepage behavior of fractured rock masses.

### 6.3 Applicability and Limitations of the Experimental Stress Path

It should be emphasized that the isotropic loading condition ($\sigma_1 = \sigma_3$) adopted in this study represents a simplified stress path and cannot fully capture fracture shear slip, asymmetric closure, or stress-induced anisotropy commonly observed under true mining stress states ($\sigma_1 > \sigma_2 > \sigma_3$).

Consequently, the conclusions drawn in this study are primarily applicable to seepage processes dominated by normal compression of tensile or mining-induced fractures, rather than shear-controlled fracture deformation.

In addition, the monotonic loading scheme employed here does not account for stress relief, cyclic loading, or repeated disturbances associated with mining operations, which may induce fracture reopening, shear slip, and seepage channel reactivation. Therefore, the present results mainly reflect the seepage evolution of fractured sandstone under sustained high-stress conditions, where permeability attenuation and stabilization are governed by progressive fracture compaction.

Future work will incorporate anisotropic and true triaxial stress paths, as well as unloading and cyclic loading conditions, to investigate the coupled effects of shear deformation, fracture reactivation, and dynamic seepage evolution. Such studies are expected to provide a more comprehensive understanding of water-conducting channel development under realistic mining-induced stress environments.

## 7 Conclusions

This study systematically investigated the seepage characteristics of single-fractured sandstone under coupled conditions of deep high-confined water and mining-induced stress through triaxial seepage experiments. The main conclusions are summarized as follows:

(1) Seepage flow and permeability decrease nonlinearly with increasing confining pressure and exhibit a pronounced threshold behavior. The most significant attenuation occurs at low confining pressures (<10 MPa), after which seepage parameters tend to stabilize. Water pressure acts as the primary driving force for seepage and shows a linear positive correlation with flow rate under constant confining pressure. At high water pressure levels (>5 MPa), the restraining effect of confining pressure is substantially weakened, indicating a strong coupling effect between the two factors.

(2) Fracture surface roughness and initial aperture jointly control seepage behavior. Fractures with lower JRC values and larger apertures exhibit higher initial seepage capacity but are more sensitive to confining pressure–induced attenuation. For fractures with identical roughness, both initial and stabilized permeability increase with aperture, following a sub-linear trend relative to the cubic law. The time-dependent permeability evolution generally follows a

rapid decay followed by stabilization, with wider fractures requiring longer times to reach equilibrium.

(3) The evolution of fracture seepage with increasing confining pressure can be categorized into three distinct stages: elastic deformation ($\sigma_3 < 4$ MPa), elasto-plastic transition (4 MPa $\leq \sigma_3 \leq$ 10 MPa), and compaction equilibrium ($\sigma_3 >$ 10 MPa). This staged behavior provides a concise framework for describing stress-controlled seepage evolution in fractured rock masses.

(4) The relationship between seepage flow and hydraulic gradient exhibits segmented characteristics, transitioning from a linear (Darcy-dominated) regime at low gradients to a nonlinear regime at high gradients. The nonlinear segment displays different deflection patterns for fractures with varying roughness, reflecting the influence of fracture structure on flow behavior.

(5) Quantitative relationships between stabilized permeability and key fracture parameters were established. Stabilized permeability shows a strong negative correlation with JRC and a positive correlation with fracture aperture, providing practical tools for predicting long-term seepage behavior of fractured rock masses.

These findings enhance the understanding of seepage evolution in fractured sandstone under complex stress–seepage coupling conditions and provide a theoretical basis for predicting water flow behavior and mitigating water inrush risks in deep mining engineering.



**Data availability**

The datasets used and/or analysed during the current study available from the corresponding author on reasonable request

**Declaration of Competing Interests**

The author declares that there is no conflict of interest regarding the publication of this article.

**Funding Declaration**

Financial support for this work is provided by the National Natural Science Foundation of China (52574176, 52474161), the Postdoctoral Research Foundation of China (2025T180509), and the Fundamental Research Funds for the Central Universities (2024ZKPYNY01).

**Authors Contribution**

H.T. and C.Z. conceived the research idea and designed the experimental framework. S.J. and S.F. were responsible for the sample preparation, including the fabrication of auxiliary splitting devices and the fracture surface characterization using 3D scanning technology. R.W. performed the triaxial seepage experiments, collected the data, and conducted the preliminary data analysis. C.Z. and H.T. developed the theoretical models and performed the in-depth analysis and interpretation of the results. The main manuscript text was written by C.Z. with significant contributions from H.T. and R.W. All authors, including S.J. and S.F., reviewed, critiqued, and approved the final version of the manuscript.

**References**

1. He, M. C., Wu, Y. Y., Gao, Y. B., & Tao, Z. G. (2024). Research progress of rock mechanics in deep mining. Journal of China Coal Society, 49(1), 75-99.
2. Wang, W. J., & GAO, F. Q. (2023). Study of the evolution of mining-induced fractures with longwall face proceeds-insight from physical and numerical modeling. Journal of Mining And Strata Control Engineering, 5(2), 023033-023033.
3. Han, P. H., Zhang, C., Wang, W. (2022). Failure analysis of coal pillars and gateroads in longwall faces under the mining-water invasion coupling effect. Eng Fail Anal, 131: 105912.
4. Liu, Y., Fang, S. X., Hu, T. F., Zhang, C., Guo, Y., Li, F. Z., Huang, J. W. (2025). Study on coupled evolution mechanisms of stress–fracture–seepage fields in overburden strata during fully mechanized coal mining. processes, 13(6): 1753.
5. Xia, B. W., Liu, S. W., Ou, C. N., & GAO, Y. G. (2022). Experimental study on mechanical properties of sandstone with single fracture under fully-mechanized top-coal caving mining stress path. Coal Science and Technology, 50(2), 95-105.
6. Zeng, X. Y., Li, B. B., Li, J. H., Duan, S. L., Ding, Y. N., & Yang, J. Song. (2025). Study on permeability mechanism of rough fractured coal considering slippage effect. Coal Science and Technology, 53□S1□□120−129.
7. Zhang, C., Wang, X. J., Han, P. H., Zhang, T., Zhang, L., Wang, F. T. (2024). Acoustic emission and splitting surface roughness of sandstone in a Brazilian splitting test under the influence of water saturation. Eng Geol, 329: 107369.
8. Li, J. W., Zhang, Y. J., Xiao, J., Li, Y. W., Zhang, Z. W. (2025). Experimental study on mechanical and fracture-seepage characteristics of sandstone under

hydro-mechanical coupling. Coal Mine Safety, 56(04): 183-194.

9. Meng, Z. P., Shi, X. C., Li, G. Q. (2016). Deformation, Failure and permeability of coal-bearing strata during longwall mining. Engineering Geology, 208: 69-80.
10. Sun, W. B., Xue, Y. C., Yin, L.M., Zhang, J. M. (2019). Experimental study on seepage characteristics of large size rock specimens under three-dimensional stress. Geomechanics and Engineering, 18(6): 567-574.
11. Lin, Z. N., Feng, S. H., Zhang, Q., & Wang, J. Q. (2023). Experimental study of triaxial shear−seepage coupling characteristics of saturated intact sandstone under high stress and high seepage pressure. Journal of Central South University (Science and Technology), 54 (06), 2419-2430.
12. Wang, G., Chen, X. C., Chen, H., Long, Q. M., & Liu, Y. X. (2025). Impacts of coal fracture roughness and aperture on the seepage of injected water: An experimental study. Coal Geology & Exploration, 53(1), 7.
13. Zhang, C., Wang, X. J., Han, P. H., Bai, Q. S., Chen, J. H. (2023). Failure analysis of residual coal pillar under the coupling of mining stress and water immersion in the goaf underground water reservoir. Environ Earth Sci, 82(12): 309.
14. Zhang, C., Huang, X. H., Wang, Y. L., Shi, X. T., Wang, F. T., Han, P. H. (2025). Simulation method and engineering application of fluid solid coupling for water immersion weakening in coal mining. Coal Science and Technology, 53(06): 407-417.
15. Lin, Z. N., Feng, S. H., Wang, J. Q., & Zang, Q. (2024). Experimental study on nonlinear flow behavior of rough single fracture under high geostress and high seepage pressure. China Civil Engineering Journal, 57 (12): 92-103+131.
16. Gan, L., Jin, H. J., Shen, Z. Z., Xu, L., Ma, H. Y. (2023). Experimental study on seepage characteristics of rough fracture of limestone under loading-unloading of confining and osmotic pressures. Chinese Journal of Geotechnical Engineering, 45(10): 2062-2071.
17. Zhao, M., & Kong, D. S. (2022). Study on seepage characteristics of rock fractures considering fracture surface roughness and opening fractal dimension. Chinese Journal of Rock Mechanics and Engineering, 41 (10): 1993-2002.
18. Liu, R. C., Jiang, Y., Li, B., Wang, X. (2015). A fractal model for characterizing fluid flow in fractured rock masses based On randomly distributed rock fracture networks. Computers and Geotechnics, 65: 45-55.
19. Jia, Q. Y., Chen, G. J., Zeng, J., Luo, X. F., Chen, Y., C. Wang, J. Z., & Xie, D. (2025). Numerical simulations of radon diffusion-seepage in single fracture of rock. Journal of Environmental Radioactivity, 284, 107643.
20. Fu, H. Y., Jiang H. B., Qiu, X., Ji, Y. P., Chen, W., Zeng, L. (2020). Seepage

characteristics of a fractured silty mudstone under different confining pressures and temperatures. J Cent South Univ, 27(7): 1907-1916.

21. Zhang, T. J., Shang, H. B., Li, S. G., Wei, W. W., Bao, R. Y., Pan, H. Y. (2018). Permeability tests of fractured sandstone with different sizes of fragments under three-dimensional stress states. Rock Soil Mech, 39(07): 2361-2370.
22. Gan, L., Liu, Y., Zhang, Z. L., Shen, Z. Z., & Ma, H. Y. (2023). Roughness characterization of rock fracture and its influence on fracture seepage characteristics. Rock and Soil Mechanics, 44(6), 1.
23. Zhang, L.M., Wang, Z. Q., Zhao, T. Y., Cong, Y. (2022). Experimental study of sandstone crack propagation behavior under different seepage pressures. Rock Soil Mech, 43(04): 901-908.
24. Chen, D., Pan, Z. J., Ye, Z. H., Hou, B., Wang. D., Yuan, L. (2016). A unified permeability and effective stress relationship for porous and fractured reservoir rocks. J Nat Gas Sci Eng, 29: 401-412.
25. Zha, H. (2020). Theory and application of seepage stability of overlying strata for shallow coal seam mining. China University of Mining and Technology.
26. Ershov, S. V., Prosviryakov, E. Y., Burmasheva, N. V., & Christianto, V. (2021). Towards understanding the algorithms for solving the Navier–Stokes equations. Fluid Dynamics Research, 53(4), 044501.